

## Macroscopic thermal diode with stable rectification ratio by thermal null medium

Hongtao Dai<sup>a,1</sup>, Fei Sun<sup>a,\*1</sup>, Hanchuan Chen<sup>a</sup>, Yichao Liu<sup>a</sup>, Yibiao Yang<sup>a</sup>, Zhihui Chen<sup>a</sup>, Shaowei Liang<sup>b</sup>, Zheng Wang<sup>b</sup>

<sup>a</sup> Key Lab of Advanced Transducers and Intelligent Control System, Ministry of Education and Shanxi Province, College of Physics and Optoelectronics, Taiyuan University of Technology, Taiyuan, 030024, China

<sup>b</sup> China-Blarus Belt and Road Joint Laboratory on Electromagnetic Environment Effect, Taiyuan, 030032, China

### ABSTRACT

Thermal diode can achieve a unidirectional and irreversible thermal transport, which can be used for direction-selective thermal management. Here we demonstrate a macroscopic thermal diode by asymmetrically embedding staggered structure of copper and expanded polystyrene sheets in stainless steel background, which can achieve a stable high thermal rectification ratio at room temperature. For the fabricated samples measured here, we observe a nearly constant thermal rectification ratio  $\sim 1.6$  at room temperature, when the temperature bias applied on both sides changes from 25 K to 50 K or the input heat power changes from 10 W to 15 W. In contrast to the conventional methods, this approach provides a new way to design macroscopic thermal diode with a stable thermal rectification effect at room temperature, which opens up new possibilities for macroscopic heat preservation, energy-saving buildings, and direction-selective thermal camouflages.

### 1. Introduction

From dealing with global warming to efficient heat dissipation in integrated circuits, many challenges facing the world today in terms of highly efficient thermal management. In many cases, it is desired that the heat flow can be directed away from the heat sensitive regions (e.g., polar or chips that need to be cooled) and then guided into the heat harvesting regions (e.g., heat recovery system and thermal batteries), where the whole process are expected as unidirectional and irreversible process, which can be referred as to direction-selective thermal management. By analogy with electric diodes, thermal diodes/rectifiers that can achieve unidirectional heat conduction and asymmetric thermal transport (i.e., thermal rectification) have important applications in direction-selective thermal transport [1–5]. For example, thermal diodes can allow components such as electronic chips to dissipate heat to the outside environment, and prevent them from being thermally damaged by high external heat sources. In addition, thermal diodes can also be used for thermal memory [6,7], stand-alone thermally driven computing systems [8], and thermal logic gates [9]. There are two operating states of the thermal diodes, forward state (conduction state) and reverse state (cut-off state), which correspond to “thermal flow can mostly pass through the thermal diode when the heat flow is fed forward” and “almost no heat flow can pass through the diode when the heat flow is fed reverse”, respectively.

So far, various types of thermal diodes based on different mechanisms have been reported, including asymmetric thermal structures created by asymmetry of geometric shape or/and material with temperature-dependent thermal conductivity (e.g., asymmetric nanostructures or mass loading) [10–13], phase change materials [14–19], transformation thermotics and memory metals [20–23],

Abbreviations: TNM, thermal null medium; EPS, expanded polystyrene.

\* Corresponding author.

E-mail address: [sunfei@tyut.edu.cn](mailto:sunfei@tyut.edu.cn) (F. Sun).

<sup>1</sup> Hongtao Dai and Fei Sun contributed equally to this work.

<https://doi.org/10.1016/j.csite.2022.102587>

Received 17 August 2022; Received in revised form 5 November 2022; Accepted 20 November 2022

Available online 28 November 2022

2214-157X/© 2022 Published by Elsevier Ltd. This is an open access article under the CC BY-NC-ND license (<http://creativecommons.org/licenses/by-nc-nd/4.0/>).

directional heat flow created by special nanostructures [24–27], and etc. [28–30]. However, the current thermal diodes that have been implemented still have some limitations. First, many thermal diodes cannot work at room temperature, i.e., high or cold temperature environment is often required due to the material/structure can only work at a specific temperature range to achieve a good thermal rectification effect [10,11,13,15,16,25,28]. Second, the thermal rectification ratios of almost all current thermal diodes are related input heat flow or temperature bias [10–20,22–25,27–30], as they involve the use of thermal materials with a temperature-dependent thermal conductivity. Third, most current thermal diodes are designed to generate thermal rectification effects at the micro/nano scale [13,16,24–26,31], and very few researches on macroscopic thermal rectification effect [17,20–23]. The reason why thermal rectification at the micro/nano level cannot be translated to the macro scale is partly due to the fact that some micro/nano-scale structures are difficult to process to macroscopic dimensions [15,31], and partly due to the fact that the environment that maintains the normal operation of the micro/nano structures (e.g., a specific temperature environment other than room temperature) cannot be satisfied at macroscopic dimensions [14–16]. Therefore, the design of macroscopic thermal diodes requires some other methods different from microscopic thermal diodes [17,20–23]. If macroscopic thermal diodes can be realized, many novel macroscopic thermal direction-selective structures can be designed for various applications, such as energy-saving walls that can allow the heat entering the building and prevent the heat leaving the building [32,33], energy-efficient air conditioning [34], and thermal management of high heat flux devices [35]. However here is still a lack of research on macroscopic diodes with stable rectification ratio, which can provide a considerable thermal rectification ratio at room temperature.

Thermal null medium (TNM) is a highly anisotropic thermally conductive medium [36] designed by transformation thermodynamics [37], which can be realized by staggered cooper and expanded polystyrene (EPS) [36,38], and achieve the directional guidance of the heat flow along the direction of the interface between copper and EPS [36,38]. Using advantage of the directional thermal conductivity of TNM, many thermal devices can be design through the “surface projection” thermal surface transformation method [36], such as thermal cloaks [36], thermal camouflages [38,39], thermal concentrators [40,41], thermal buffering [42], thermal rotator [43], etc. In this study, a passive macroscopic thermal diode with stable rectification ratio is designed by asymmetrically placing strip-shaped TNM units (staggered structure of copper and EPS) in background medium with homogenous thermal conductivity (see Fig. 1). Compared with most existing thermal diodes, the diode can achieve a good thermal rectification effect at room temperature, i.e., it can work without any additional energy supply to maintain its operating temperature. After optimization of the structural parameters, its rectification ratio can reach 1.96, which is basically at the same level as the existing partial thermal diodes. In addition, the rectification ratio of the designed thermal diode will remain unchanged when the power of input heat flow or temperature bias is changed, which exhibits a stable thermal rectification effect.

## 2. Method and results

### 2.1. Simplified TNM unit

The thermal diode in Fig. 1a is designed by asymmetrically embedding six strip-shaped 2D TNM units in the background medium. Each strip-shaped 2D TNM unit has the same structure, i.e., staggered structure of copper-EPS sheets (see Fig. 1c), which can

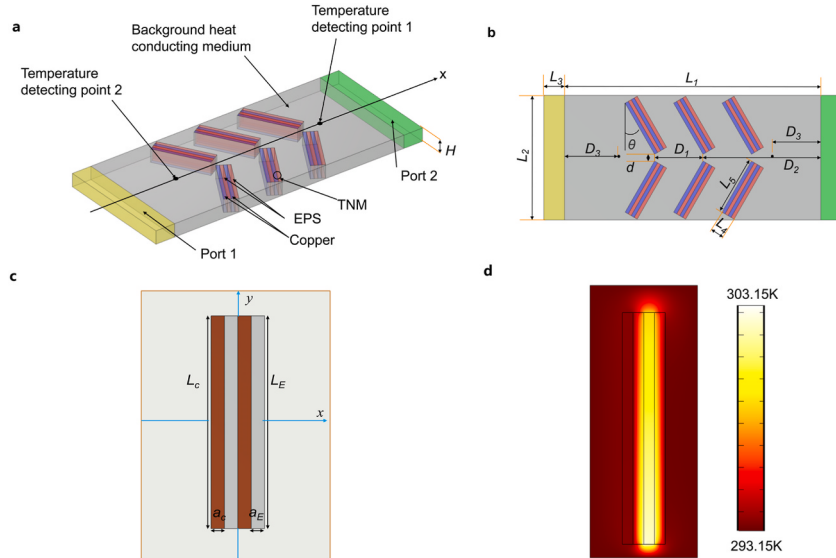


**Fig. 1.** The schematic diagram of the designed thermal diode based on TNM units. (a) is perspective view of 3D structure of the designed diode. (b) is top view of the designed diode in (a). The gray area is the background medium and the white region outside the diode is air. (c) The schematic diagram of copper-EPS array in the background medium, which performs as a simplified 2D TNM unit. (d) The 2D simulated temperature distribution when a high temperature source with temperature 303.15 K is set on the center of the lower surface of the staggered copper-EPS sheets. The rectangular boundary of the calculation domain is set as constant low temperature 293.15 K. The high temperature source is chosen as a line heat source whose length is  $a_c/10$ .

directionally guide thermal flux along the direction of the interface between copper and EPS [36,38]. The TNM units are covered by air on the top and bottom surfaces in Fig. 1a, which almost does not conduct heat ( $\kappa_{\text{air}} = 0.024 \text{ W}/(\text{m}\cdot\text{K})$ ) [44] and can be modeled as the thermally insulated boundary. Therefore, the strip-shaped TNM units can be modeled as 2D TNM units, i.e., we only need to consider its effective thermal conductivity within its surface.

Taking one of the six identical 2D TNM units in Fig. 1a as an example, the local coordinate system  $x$ - $y$  is set in Fig. 1c. Each 2D TNM unit consists of two copper sheets and two EPS sheets of equal length  $L_c = L_E$ . The widths of copper sheets and EPS sheets are  $a_c$  and  $a_E$ , respectively. The effective thermal conductivity of 2D staggered structure of copper-EPS sheets can be derived based on effective medium theory [45], which can be expressed as:

$$\begin{cases} \frac{1}{\kappa_x} = \frac{f_c}{\kappa_c} + \frac{f_E}{\kappa_E} \\ \kappa_y = \kappa_c f_c + \kappa_E f_E \end{cases}, \quad (1)$$

where  $f_c = a_c/(a_c + a_E)$  and  $f_E = a_E/(a_c + a_E)$  are filling factors of copper sheets and EPS sheets, respectively. The anisotropic thermal conductivity of the 2D staggered structure of copper-EPS sheets can also be expressed in matrix as:

$$\kappa = \begin{pmatrix} \frac{\kappa_c \kappa_E}{\kappa_c f_c + \kappa_E f_E} & 0 \\ 0 & \kappa_c f_c + \kappa_E f_E \end{pmatrix}. \quad (2)$$

In our design  $a_c = a_E$ , which means  $f_c = f_E = 0.5$  in Eq. (2). The effective thermal conductivity of the 2D staggered structure of copper-EPS sheets in Eq. (2) can be further reduced to:

$$\kappa = \begin{pmatrix} \frac{2\kappa_c \kappa_E}{\kappa_c + \kappa_E} & 0 \\ 0 & \frac{\kappa_c + \kappa_E}{2} \end{pmatrix} = \sqrt{\kappa_c \kappa_E} \begin{pmatrix} \frac{2\sqrt{\kappa_c \kappa_E}}{\kappa_c + \kappa_E} & 0 \\ 0 & \frac{\kappa_c + \kappa_E}{2\sqrt{\kappa_c \kappa_E}} \end{pmatrix}. \quad (3)$$

The thermal conductivities of copper and EPS are  $\kappa_c = 401 \text{ W}/(\text{m}\cdot\text{K})$  and  $\kappa_E = 0.03 \text{ W}/(\text{m}\cdot\text{K})$ , respectively [46,47]. If background medium is chosen as 40% nickel steel, whose thermal conductivity is  $\kappa_0 = 10 \text{ W}/(\text{m}\cdot\text{K})$  [48], the effective thermal conductivity of the 2D staggered structure of copper-EPS sheets in Eq. (3) can be expressed as:  $\kappa = \kappa_0 \text{diag}(0.006, 20.0515)$ .

Considering the simplified thermal conductivity of TNM, i.e., much greater than the thermal conductivity of the background medium along main axis and close to zero in other orthogonal directions [36,38], the 2D staggered structure of copper-EPS sheets whose effective thermal conductivity is  $\kappa = \kappa_0 \text{diag}(0.006, 20.0515)$  can perform as simplified 2D TNM unit whose main axis is along the direction of copper-EPS's interface.

From the Fourier's law for anisotropic media  $\bar{q} = -\bar{\kappa} \nabla T$  ( $q$  is the flow of heat energy per unit area,  $\kappa$  is anisotropic thermal conductivity, and  $T$  is the temperature), we can analyze the direction of heat flow in each simplified 2D TNM unit. For the simplified 2D TNM unit in Fig. 1c whose thermal conductivity can be expressed as  $\kappa = \kappa_0 \text{diag}(0.006, 20.0515)$ , the heat flow can be calculated as  $\bar{q} \sim -\kappa_0(0.006 \partial_x T \hat{x}_0 + 20 \partial_y T \hat{y}_0) \sim -\kappa_0 20 \partial_y T \hat{y}_0$ , which shows the heat flow is basically restricted to propagate along the direction of the TNM's main axis.

Numerical simulations verify the designed 2D staggered structure of copper-EPS sheets can perform as a simplified 2D TNM unit, which can directionally guide the heat flux along the direction of copper-EPS's interface in Fig. 1d. As shown in Fig. 1d, if a high temperature source is located on one surface of the staggered structure of copper-EPS sheets, the heat flux produced by the thermal source will be guided along the direction of copper-EPS's interface, and a thermal image is created on the other surface of the copper-EPS sheets.

## 2.2. The design of initial structure for thermal rectification

As shown in Fig. 1, the thermal diode is designed by asymmetrically embedding six strip-shaped 2D TNM units in background medium with homogeneous thermal conductivity  $\kappa_0$ . The 2D TNM unit is composed by staggered structure of copper-EPS sheets, which can directionally guide thermal flux along the direction of the interface between copper and EPS [36,38]. If the filling factors of copper sheets and EPS sheets are the same, the effective thermal conductivity of staggered structure of copper-EPS sheets can be expressed by Eq. (3):

In order to make the copper-EPS sheets embedded in the background medium as close as possible to the theoretical TNM [36], the conductivity of the background material is expected to be the geometric mean of the thermal conductivity of copper and EPS,

$$\kappa_0^2 = \kappa_c \cdot \kappa_E, \quad (4)$$

where  $\kappa_0$  is the thermal conductivity of the background medium material. In this case, the effective thermal conductivity of staggered structure of copper-EPS sheets embedded in the homogeneous thermally conductive background medium in Eq. (3) can be further written as:

$$\kappa = \kappa_0 \text{diag} \left( \frac{2\kappa_0}{\kappa_c + \kappa_E}, \frac{\kappa_c + \kappa_E}{2\kappa_0} \right). \quad (5)$$

Eq. (5) shows the two principal values of this anisotropic thermal conductivity are the reciprocal of each other, which exactly matches the requirement of TNM's parameters [36]. In addition,  $2\kappa_0/(\kappa_c+\kappa_E)\gg 1$  and  $(\kappa_c+\kappa_E)/(2\kappa_0)\ll 1$ , which is consistent with the material parameters required for the simplified 2D TNM and indicates the main axis of the 2D TNM unit is the direction of the interface between copper and EPS.

The working principle of the thermal diode based on the structure in Fig. 1 can be explained as follow: If Port 1 is set as a high temperature source that input a constant thermal power to the thermal diode, and Port 2 is set as a low temperature source with constant temperature, most of the heat flow will be guided by TNM units to gather around the  $x$ -axis, and then propagate from port 1 to port 2. In this case, there is little convective heat loss with the air at the boundary of the structure during the transmission process, and most of the heat flow is guided to Port 2, which corresponds to the forward state of the thermal diode (see Fig. 2a and Supplementary Movie 1). Conversely, if the heat flow is input from Port 2, i.e., Port 2 is set as a high temperature source with a constant output power, and Port 1 is set as a low temperature source with constant temperature, most of the heat flow is guided by the TNM units to the edge of the thermal diode that is away from the  $x$ -axis, and then propagate from port 2 to port 1. In this case, most of the heat power is lost due to the convection with air at the edge of the thermal diode, and almost no heat power transfer from Port 2 to Port 1, which corresponds to the reverse state of the thermal diode (see Fig. 2b and Supplementary Movie 1). Fig. 2c and d shows the distribution of heat flows when the thermal diode work in the forward state and the reverse state, respectively, which further verifies the directional thermal conduction achieved by each 2D TNM unit in the entire thermal diode. It can be seen that the well-designed thermal diode with asymmetrically placed TNM units can conduct the heat flows to the other side by converging them to the center of the structure in forward state, and prevent the heat flows from reaching the other side by spreading them to the air convection loss boundaries in the reverse state. In the above process, no other form of energy supply is required, and there are no requirements on the temperature of the environment. Therefore, the initial structure designed in Fig. 1 can perform as a passive thermal diode at room temperature.

The thermal rectification ratio  $R$  is usually used to quantitatively measure the performance of thermal diodes, which is defined as follow [11,14]:

$$R = \frac{|J_F|}{|J_R|}, \quad (6)$$

where  $J_F$  and  $J_R$  represent heat flux density received at the output port of the diode when it works in forward state and reverse state, respectively. After reaching the thermal steady state, by measuring the temperatures of the detecting points 1 and 2, respectively,  $J_F$  and  $J_R$  can be calculated (see Supplementary note 2). For the initial structure in Fig. 2, the thermal rectification ratio calculated by Eq. (6) is  $R = 1.59$ .

### 2.3. Structural optimization and stable thermal rectification ratio

In order to reach the optimal thermal rectification ratio  $R$ , the effect of different structural parameters on the thermal rectification ratio  $R$  is numerically studied (see Fig. 3). In the optimization, the overall sizes of the thermal diode are fixed (see Supplementary Note 1), only the structural parameters of the TNM units and detecting points are changed, and the angle between the TNM unit and the  $x$ -axis is limited to  $0^\circ \leq \theta \leq 90^\circ$ .

As shown in Fig. 3a-d, once the structural parameters are given, the thermal rectification ratio  $R$  of the designed thermal diode remains unchanged no matter how the input heat power changes, i.e., thermal rectification ratio is independent of the input heat power and temperature bias, which cannot be achieved by most of thermal diodes that have been reported so far [10–20,22–25, 27–29]. This is attributed to the temperature insensitivity of the thermal conductivity of the designed thermal diode, i.e., the thermal conductivity of copper-EPS sheets and background medium (nickel steel or stainless steel) are almost invariant with input heat power and temperature (see Supplementary Note 1), which leads to the directional thermal conducting property of TNM is effective over a

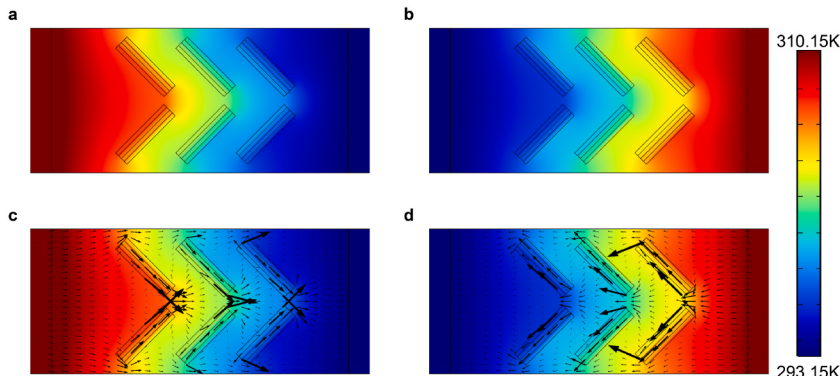


**Fig. 2.** The 2D simulated surface temperature distribution of the initial structure for forward state (a) and reverse state (b), respectively. The calculated heat flows (the black arrows) in each point of the designed thermal diode for forward state (c) and reverse state (d), respectively. The length and the direction indicate the magnitude and the direction of the heat flow, respectively. In this initial structure, some structural parameters are chosen as  $\theta = 45^\circ$ ,  $L_5 = 85$  mm,  $D_1 = 75$  mm,  $D_2 = 155$  mm, and  $D_3 = 50$  mm. Other parameters and numerical settings can be found in Supplementary Note 1.

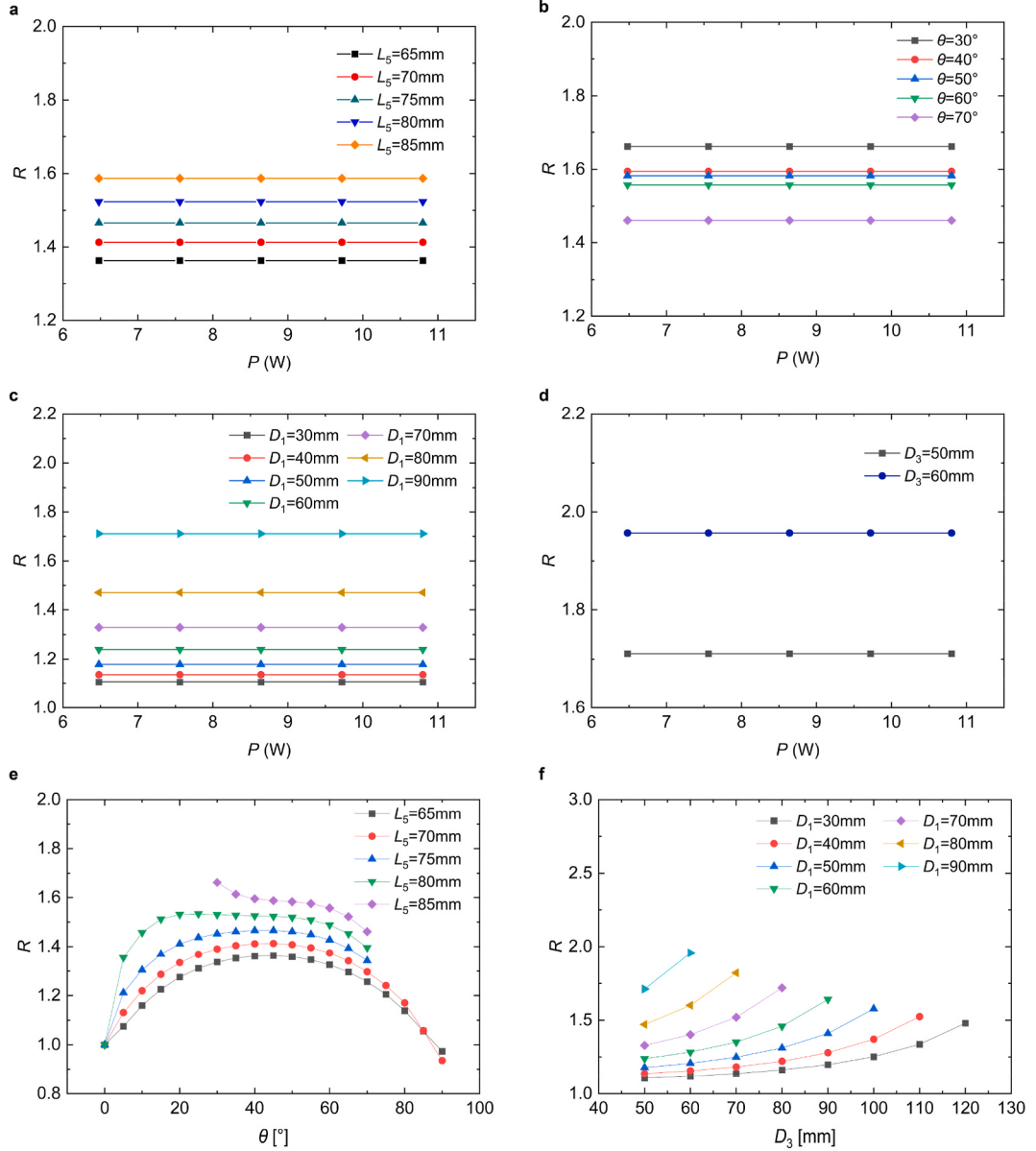


**Fig. 3.** The relation between the input heat power  $P$  and thermal rectification  $R$  for various structural parameters of the thermal diode. (a)  $P$ - $R$  curve when the length of the TNM units  $L_5$  chooses different values, while keeps other parameters unchanged, i.e.,  $\theta = 45^\circ$ ,  $D_1 = 75$  mm,  $D_2 = 155$  mm,  $D_3 = 50$  mm. (b)  $P$ - $R$  curve when the inclination angle of the TNM units  $\theta$  chooses different values, while keeps other parameters unchanged, i.e.,  $L_5 = 85$  mm,  $D_1 = 75$  mm,  $D_2 = 155$  mm,  $D_3 = 50$  mm. (c)  $P$ - $R$  curve when the distance between two TNM units  $D_1$  chooses different values, while keeps other parameters unchanged, i.e.,  $L_5 = 85$  mm,  $\theta = 30^\circ$ ,  $D_2 = 175$  mm,  $D_3 = 50$  mm. (d)  $P$ - $R$  curve when the length of the distance between the temperature detecting point and the constant temperature source  $D_3$  chooses different values, while keeps other parameters unchanged, i.e.,  $L_5 = 85$  mm,  $\theta = 30^\circ$ ,  $D_2 = 175$  mm,  $D_1 = 90$  mm. (e)  $R$ - $\theta$  curve when the length of the TNM units  $L_5$  chooses different values, while keeps other parameters unchanged, i.e.,  $D_1 = 75$  mm,  $D_2 = 155$  mm,  $D_3 = 50$  mm. (f)  $D_3$ - $R$  curve when the distance between two TNM unit  $D_1$  chooses different values, while keeps other parameters unchanged, i.e.,  $L_5 = 85$  mm,  $\theta = 30^\circ$ ,  $D_2 = 175$  mm. The other numerical settings can be found in Supplementary Note 1.

wide range of input heat power and temperature variations. While the thermal conductivity of materials or the unidirectional thermal conducting property of other thermal diodes are sensitive to temperature variations, resulting in effects that the thermal rectification ratio  $R$  of other thermal diodes is often dependent on temperature and input heat power [10–20,22–25,27–29].

In order to explore the physical mechanism of how each geometric parameter affects  $R$ , more combined numerical simulation results are presented in Fig. 3e and f. Due to the geometric constraints  $L_2 \geq 2L_5\cos\theta + 2L_4\sin\theta + d$  and  $L_1 \geq D_3 + D_2 + D_1 + (D_2 - D_1 - L_4\cos\theta) + L_5\sin\theta$ , the different color curves in Fig. 3e and f take different numbers of prints, and geometry parameters cannot take values freely. It can be seen from Fig. 3e that no matter what the value of  $\theta$  is, the  $L_5$  and  $R$  satisfy a positive correlation, which can also be seen from Fig. 3a: if other structural parameters are fixed (i.e.,  $\theta = 45^\circ$ ,  $D_1 = 75$  mm,  $D_2 = 155$  mm,  $D_3 = 50$  mm), the larger the

length of the TNM units  $L_5$ , the larger the thermal rectification ratio  $R$ . In forward state, the TNM units with the larger length  $L_5$  can capture and guide more the input heat flow along the main axis of the TNM units to gather around the  $x$ -axis, which leads to the less convective heat loss at the edges of the thermal diode and the larger power of output heat flux density  $J_F$ . In reverse state, the TNM units with the larger length  $L_5$  can capture and guide more input heat flow to the edge of the thermal diode, which leads to more convective heat loss due to the convection with air and the smaller power of output heat flux density  $J_R$ . Therefore, the larger length of the TNM unit  $L_5$  can provide a larger thermal rectification ratio  $R$ .

It can be seen from Fig. 3e that the relationship between  $\theta$  and  $R$  is not a positive correlation, which is also related to  $L_5$ ; if  $L_5$  is small (e.g.,  $L_5 \leq 75$  mm), the geometric constraint between  $\theta$  and  $L_5$  are not obvious, which means  $\theta$  can take all values from  $0^\circ$  to  $90^\circ$ . In this case, each TNM unit is far from the edge of the diode (i.e., the edge effect is small) and the asymmetric effect mainly affects the thermal rectification ratio  $R$ . For small  $L_5$ , the thermal rectification ratio reaches the maximum when  $\theta = 45^\circ$  (see Fig. 3e), which corresponds to the max asymmetry of the TNM units at this time and results in the heat flow asymmetry to the maximum degree. If  $L_5$  is small (e.g.,  $L_5 \geq 75$  mm), Take Fig. 3b as an example, the geometric constraint between  $\theta$  and  $L_5$  should be considered, which means  $\theta$  cannot take all values from  $0^\circ$  to  $90^\circ$ . In this case, TNM units are close to the edge of the diode, which means both edge effect and asymmetry effect will influence when the best thermal rectification ratio  $R$  can be obtained. Once the end of each TNM unit is closer to the diode's edge, the larger convective heat loss will be generated in reverse state, and the more concentrated heat flows are gathered around the  $x$ -axis in forward state, which is referred to as the edge effect. For large  $L_5$ , the  $\theta$  corresponding to the maximum thermal rectification ratio is not  $45^\circ$  (see Fig. 3b and e), which shows that the edge effect cannot be ignored and the asymmetric effect is no longer the unique factor affecting  $R$ . In order to obtain the best  $R$ , both  $\theta$  and  $L_5$  should be considered together, which reflect the influence of the edge effect and asymmetric effect, respectively.

It can be seen from Fig. 3f that no matter what the value of  $D_1$  is, the relationship between  $D_3$  and  $R$  is a positive correlation, which can also be seen from Fig. 3c: the longer the distance between two TNM pairs  $D_1$ , the larger the thermal rectification ratio  $R$  when other parameters are fixed (i.e.,  $L_5 = 85$  mm,  $\theta = 30^\circ$ ,  $D_2 = 175$  mm,  $D_3 = 50$  mm). In forward state, input heat flow at the edge of the diode will be guided by the first TNM pairs to propagate around the  $x$ -axis (i.e., convective heat loss at the edge is mainly reduced by the first TNM pairs), and the TNM pairs in the later cascade do not contribute much to the reduction of convective heat loss. Therefore, the distance between TNM pairs  $D_1$  has little influence on power of forward heat flux density  $J_F$ . In reverse state, input heat flow is first dispersed to the edge after passing through the first TNM pairs (resulting in the first convective heat loss), and then, it is dispersed through the next cascade of TNM pairs after thermal diffusion for a distance  $D_1$  (resulting in the second convective heat loss), and it continues in this manner for the next TNM pairs. In this process, the longer the distance between two adjacent TNM pairs  $D_1$ , the better the thermal diffusion after passing through the front TNM pairs, and the more convective heat loss at the later TNM pairs, which makes  $J_R$  smaller. Since the larger the distance between TNM pairs  $D_1$  can lead to a smaller  $J_R$  while  $J_F$  is almost unchanged, this eventually leads to a larger thermal rectification ratio  $R$  (see Eq. (6)).

Fig. 3f also shows that the relationship between  $D_1$  and  $R$  is a positive correlation for different values of  $D_3$ , which can also be seen from Fig. 3d: once other structural parameters fixed (i.e.,  $L_5 = 85$  mm,  $\theta = 30^\circ$ ,  $D_2 = 175$  mm,  $D_1 = 90$  mm), the shorter the distance between the temperature detecting point and the constant temperature source  $D_3$ , the smaller the thermal rectification ratio  $R$ . This is

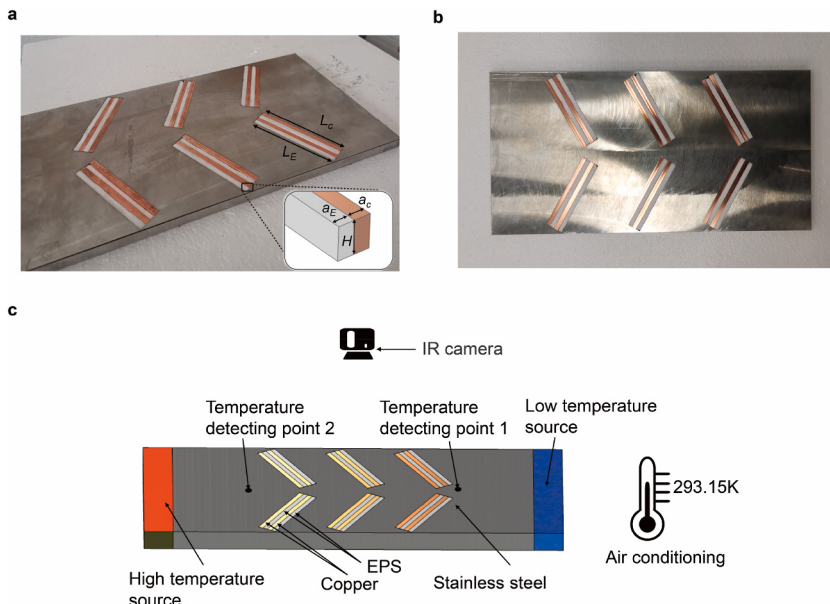
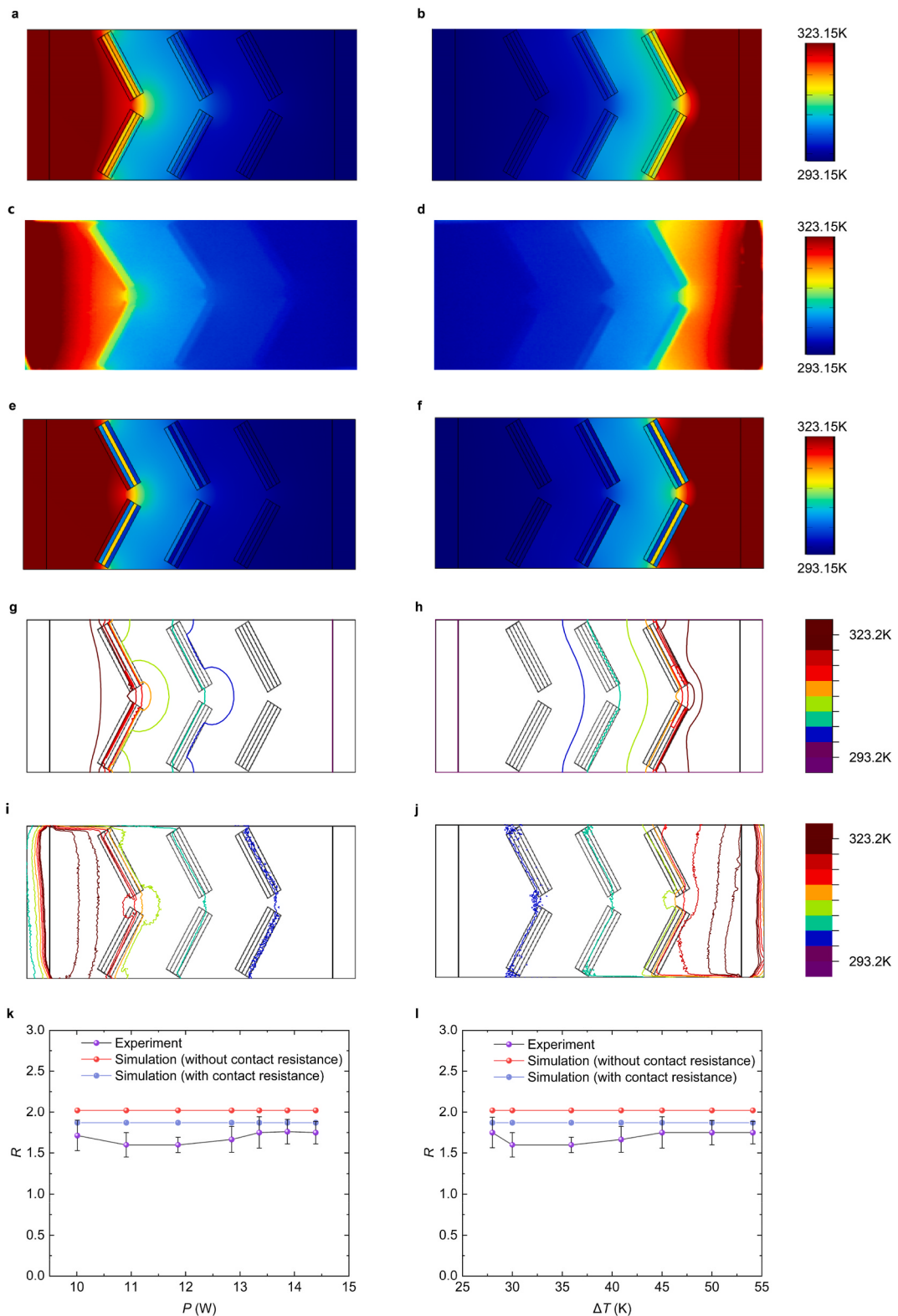


**Fig. 4.** Photograph of the fabricated sample (a), (b) and schematic diagram of the experimental measurements (c). (a) and (b) are side and top view of the sample, respectively. The enlarged illustration shows the details of the TNM unit. (c) is schematic diagram of the experimental measurements. In this showcase, the thermal diode works in forward state, while the high temperature source and the cold source need to exchange position when the thermal diode works in reverse state.



(caption on next page)

**Fig. 5.** The simulated temperature field distribution and the measured temperature field distribution of the optimized thermal diode in forward state and reverse state, respectively. The simulated surface temperature field distribution of the optimized thermal diode operating in forward state (a) and in reverse state (b), respectively. The measured surface temperature field distribution of the optimized thermal diode operating in forward state (c) and in reverse state (d), respectively. The parameter settings in experiment (c) and (d) are consistent with the parameter settings in simulation (a) and (b), which can be found in Supplementary Note 1. The simulated surface temperature field distribution of the optimized thermal diode with contact resistance operating in forward state (e) and in reverse state (f), respectively. (g)–(j) are the corresponding temperature contours of (a)–(d). (k) and (l) are measured/simulated P-R and  $\Delta T$ -R curves for the optimized thermal diode, respectively. The measured uncertainties are also indicated by error bar of rectification in (k) and (l), which is elaborated in Supplementary Note 4.

due to the fact that  $D_3$  implicitly affects the temperatures of two detecting points  $T_1$  and  $T_2$ , which together with the constant temperature of the low temperature source  $T_L$  determine the magnitude of  $R$  (see Eq. (S3) in Supplementary Note 2). As  $D_3$  decreases, temperature detecting points are closer to the constant low temperature source. In this case, the temperature of two detecting points  $T_1$  and  $T_2$  are closer to the constant low temperature  $T_L$  ( $T_1 \sim T_2 \rightarrow T_L$ ), the temperature difference between  $(T_1 - T_L)$  and  $(T_2 - T_L)$  becomes smaller, and thus the thermal rectification ratio  $R$  becoming worse (see Eq. (S3) in Supplementary Note 2).

After extensive numerical simulations, an optimized structure with the maximum thermal rectification ratio  $R = 1.96$  can be obtained, when the corresponding structural parameters are selected as  $\theta = 30^\circ$ ,  $L_5 = 85$  mm,  $D_1 = 90$  mm,  $D_2 = 175$  mm,  $D_3 = 60$  mm.

### 3. Experimental design and measurement results

To experimentally verify the thermal rectification effect of the designed thermal diode, a thermal diode base on the optimized structural parameters in the simulation is fabricated (see the photograph of the fabricated sample in Fig. 4a and b). The fabricated sample is composed of the copper-EPS sheets ( $a_c = a_E = 5$  mm,  $H = 10$  mm, and  $L_c = L_E = 85$  mm) embedding in the stainless steel ( $L_1 = 370$  mm,  $L_2 = 180$  mm,  $H = 10$  mm, and  $\kappa_0 = 14.2$  W/(m•K) [49]), which is the closest material to the thermal conductivity required by Eq. (4) that can be purchased. The schematic diagram of the experimental measurements is shown in Fig. 4c, where the entire experimental setup is located in a closed room, and the room temperature is maintained at 293.15 K by air conditioning. The high temperature source is a thermal resistance heater supplied by a constant current source, which can provide a heat flow output with constant thermal power. The low temperature source is a copper plate connected with a constant temperature metal bath, which can provide a constant temperature  $T_L = 293.15$  K (see Supplementary Movie 2). The experimental measurements can be divided into three steps: heat power measurement in forward state, heat power measurement in reverse state, and rectification ratio calculation.

In the first step, high and low temperature sources are fixed at port 1 and port 2 of the sample (see Figs. 1a and 4c), and adjusted to create an output heat flow with constant power  $P = 11.86$  W and a constant temperature  $T_L = 293.15$  K, respectively. Then, the temperature distribution on the sample surface is captured by IR camera (FOTRIC 288, whose temperature accuracy is 2%), which changes with time. After about 2 h, the temperature distribution on the sample surface no longer changes, i.e., the thermal steady state is reached. Due to the large volume occupied by the sample and the low thermal conductivity of its main part (i.e.,  $\kappa_0 = 14.2$  W/(m•K) for the stainless-steel plate occupying 85% of the sample's volume), as well as the heat loss due to air convection and thermal radiation when the heat flow travels through the sample, it takes a long time for the heat to diffuse in the sample. In addition, the power created by the heat source is low (only 14.39 W) and will be further reduced due to the heat exchange with the air before it enters the sample, which results in a very low power of heat flow incidents onto the sample. Thus, the experiment takes long time (~2 h) to reach steady state. At this time, the surface temperature field distribution on the sample surface is recorded by IR camera (see Fig. 5c), from which the temperature at the detecting point 1 can be obtained. Next, the power of the heat flux density received at the output port of the diode in forward state  $J_F$  can be calculated from the temperature at the detecting point 1 (see Supplementary Note 2).

In the second step, after waiting about 1 h until the whole system cools down, the position of high temperature source and low temperature source are exchanged with each other. Then, after supplying energy to the high/low temperature sources, and waiting for about 2 h until the system reaches the thermal steady state, the temperature field distribution on the sample surface is recorded again by IR camera (see Fig. 5d), from which the temperature at the detecting point 2 can be obtained. Next, the power of the heat flux density received at the output port of the diode in reverse state  $J_R$  can be calculated from the temperature at the detecting point 2 (see Supplementary Note 2).

In the third step, the thermal rectification ratio  $R = 1.6$  can be calculated by Eq. (6) since  $J_F$  and  $J_R$  have been obtained in previous two steps. More details of the measurement process can be found in Supplementary Note 3 and Supplementary Movie 3. The experimental measured temperature distributions (Fig. 5c and d) are consistent well with the 3D simulations (Fig. 5a and b), which also verifies the expected good thermal rectification effect. In addition, the corresponding temperature contours of Fig. 5a–d are plotted in Fig. 5g–j, which further verify the expected thermal rectification effect: the contour lines are modulated according to the distribution of TNM units, which shows a much higher temperature at the center of the diode's output port in the forward state than in the reverse state, and results in the expected thermal rectification ratio  $R$  (see Eq. (S3) in Supplementary Note 2).

Next, additional experimental measurements are made to verify the stable thermal rectification ratio of the fabricated thermal diode. The steps for each experimental measurement of rectification ratio  $R$  remain the same as the three steps described above, except that the constant output thermal power of the high temperature source  $P$  is adjusted to 10.01 W, 10.91 W, 12.85 W, 13.35 W, 13.87 W and 14.39 W, respectively, in each measurement (see Supplementary Movie 2). The measured and simulated P-R curves are shown in Fig. 5k, which shows the thermal rectification  $R$  hardly changes with output thermal power  $P$ , i.e., the diode designed is very stable. As the output thermal power of the high temperature source  $P$  changes (low temperature source remains constant temperature  $T_L = 293.15$  K), the temperature bias  $\Delta T$  at both ports of the diode at thermal steady state will also change, therefore the stability of the diode can also be tested by whether  $R$  changes under different bias  $\Delta T$ . The measured and simulated  $\Delta T$ -R curves are shown in Fig. 5l, which also verifies that the designed thermal diode has very good stability (see Supplementary Note 5 for more quantitative

descriptions of the stability).

In the heat transfer process of heat flow through the designed thermal diode, the effective thermal resistance mainly includes thermal spreading resistance and contact thermal resistance. The spreading resistance only occurs when thermal energy is transferred from a small area to a larger area in a substance with finite thermal conductivity [50,51], as the heat source is set to be uniform in the simulation and adopts a uniform distribution of resistance wires in the experiment. However, the contact thermal resistance can not be ignored after research. For the simulated results in Fig. 5a and b, where the contact resistance is not considered (i.e., the EPS and the copper are perfect contact), which causes that the measured surface temperatures in Fig. 5c and d are slightly lower than the simulated surface temperatures in Fig. 5a and b. If the contact resistance is introduced (i.e., the copper and the EPS are not in perfect contact), the corresponding simulated temperature distributions are shown in Fig. 5e and f, which shows that the measured surface temperatures in Fig. 5c and d are much closer to the simulated surface temperatures with contact resistance in Fig. 5e and f.

Although the actual high temperature source (i.e., nickel-chromium resistance wire) is set to the same output thermal power in the experiment as in the simulation, the high temperature resistance wire in the experiment will inevitably produce convective heat dissipation with the surrounding air, which results in the actual thermal power into the heat diode in the experiment being slightly less than the simulated setting. The convective heat dissipation and contact resistance are the reasons why the measured surface temperatures in Fig. 5c and d are slightly lower than the simulated surface temperatures in Fig. 5a and b.

In order to analyze the reasons for the small deviation of the simulated curve from the experimental curve in Fig. 5k and l, we use the simulated result in Fig. 5a and b as the perfect case with minimum losses, and then different loss factors are introduced one-by-one numerically to analyze the percentage contribution of each factor (e.g., contact thermal resistance, air convection, etc.) to the difference between simulation and experiment. To quantitatively describe the contribution of each factor to the deviation, the percentage contribution can be defined as  $\delta = (R_{\text{before}} - R_{\text{after}}) / (R_{\text{perfect}} - R_{\text{measured}})$ , where  $R_{\text{before}}$  is the simulated rectification ratio before one loss factor is introduced,  $R_{\text{after}}$  is the simulated rectification ratio after one loss factor is introduced,  $R_{\text{Perfect}}$  is the rectification ratio for the perfect case in Fig. 5a and b and  $R_{\text{measured}}$  is the average measured rectification ratio in experiment.

Fig. 6a shows the modified simulated  $R$  when different loss factors are introduced one-by-one, and Fig. 6b gives the percentage contribution of each factor on the rectification ratio  $R$ . When the contact thermal resistance is considered, the simulated rectification ratio (light blue curve) reaches closer to the measured curve (black curve) in Fig. 6a, which contributes  $\delta = 45.53\%$  to the deviation between measured and simulated results (see Fig. 6b). In the experiment, Teflon is added to the upper surface of the sample to eliminate the inaccuracy of the measured temperature field distribution by IR camera due to the different surface emissivities of different materials, and a foam pad is placed under the sample to hold/fix it. However, these will lead to a smaller air convection coefficient at different locations of the sample in the experiment compared to the settings in the simulation, i.e., the bad air convection. Based on the consideration of contact resistance, if the bad air convection is introduced in simulations (convection coefficient changed from 5 to 2 [ $\text{W}\cdot\text{m}^{-2}\cdot\text{K}^{-1}$ ]), the simulated rectification ratio  $R = 1.7729$  (blue curve) will be much closer to the measured curve (black curve) in Fig. 6a, and its percentage contribution is  $\delta = 29.74\%$ . During the experiment, the ambient temperature in our laboratory may be slightly higher than 293.15 K due to the heat dissipation of the surrounding experimental devices. Based on the consideration of contact resistance and bad air convection, if the slight ambient temperature rise is introduced (i.e., 2° higher than the perfect case) in simulations, the simulated rectification ratio  $R = 1.7092$  (gray curve) will almost match the measured curve (black curve) in Fig. 6a, and its percentage contribution is  $\delta = 19.43\%$ . The remaining small part of the percentage contribution 5.3% is due to other factors that cannot be modeled in simulations, which include sample processing error, experimental measurement deviation, inhomogeneous air convection and ambient temperature.

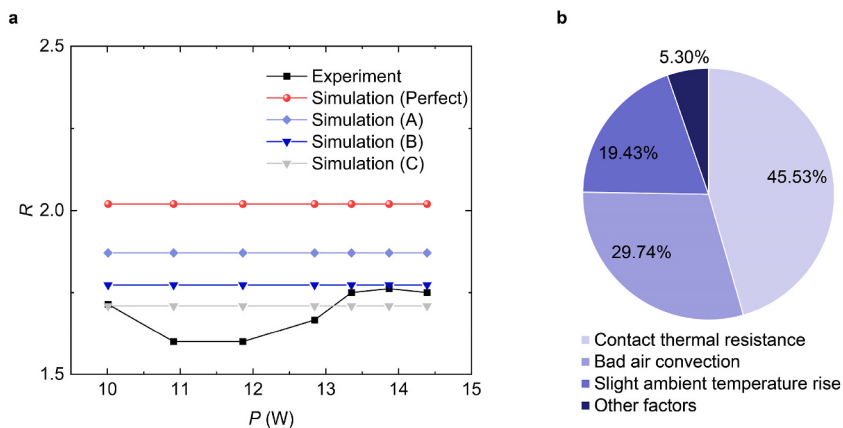


Fig. 6. (a) Is measured/simulated  $P$ - $R$  curves for different cases: the setting of simulation (Perfect) are the same as Fig. 5a and b; the simulation (A) adds contact thermal resistance to the simulation (Perfect) (the contact thermal resistance is set to add an air layer in the contact gap, and the air thermal conductivity is 0.024 [ $\text{W}\cdot\text{m}^{-2}\cdot\text{K}^{-1}$ ]); the simulation (B) changes the convection coefficient  $h$  from 5 to 2 [ $\text{W}\cdot\text{m}^{-2}\cdot\text{K}^{-1}$ ] on the basis of the simulation (A); the simulation (C) changes the external temperature from 293.15 K to 295.15 K based on the simulation (B). (b) is the percentage contribution chart of each factor on the rectification ratio  $R$ .

#### 4. Discussion

In recent years, some thermal diode-like black box, which can create a macroscopic asymmetry of the heat flow transmitted from two opposite directions and provide very high transient rectification ratio, has been proposed by smartly combining thermal concentrator (energy harvesting unit) and thermal cloak (energy shielding unit) derived from transformation thermotics [21]. However, the thermal diode-like black box with more than two ports (actually a four-port multi-pole tube) is not a thermal diode in the strict sense, as it cannot achieve the switching between the forward state and the reverse state directly by exchanging the direction of heat flow between the two fixed ports (it has to introduce some other ports to achieve this). The thermal diode-like black box with high transient rectification ratio may have its special applications for 3D bulk thermal controlling, which is slightly different from conventional thermal diodes. The thermal diode proposed in this study has only two ports and can provide the switching between the forward state and the reverse state directly by simply changing the direction of the input heat flux, which can be treated as a strictly thermal diode. The designed thermal diode in this study is a surface plate structure, which is more suitable for some on-chip thermal control.

In order to solve the existing problems of thermal diodes with unstable thermal rectification ratios, inability to operate at room temperature, and the usual need to use micro/nano structures or special materials, a novel macroscopic thermal diode is designed and fabricated in this study by asymmetrically embedding TNM units in the background medium. Based on the directional thermal projecting feature of TNM, asymmetrically placing strip-shaped TNM units in homogenous background medium can lead to the fact that the convective flows with air at the edge of the structure are different when the heat flows incident from the opposite directions, which performs as a novel thermal diode. By introducing various geometrical parameters of the designed thermal diode (e.g., the inclination angle of the TNM units  $\theta$ , the length of the TNM unit  $L_5$ , the distance between two TNM pairs  $D_1$ , and etc.), numerically results show the thermal rectification ratio  $R$  is changed correspondingly. After about 130 numerical simulations (each time only one geometrical parameter is scanned and other geometrical parameters are fixed), the best thermal rectification ratio  $R \sim 2$  is obtained. An optimized thermal diode is fabricated, whose thermal rectification ratio  $R \sim 1.6$  is measured in the experiment, which is basically the same level of magnitude as most existing thermal diodes. Compared with other existing thermal diodes, the proposed thermal diode in this study can provide a stable rectification effect at room temperature, which does not require complex materials and micro-nano structures. Both simulated and measured results show the proposed thermal diode can provide a good thermal rectification ratio at the room temperature, which does not change with the input thermal flow or temperature bias. The proposed thermal diode may provide a new way for macroscopic direction-selective thermal management, e.g., heat preservation device, energy-saving buildings, and direction-selective thermal camouflages.

#### Author contributions

H. D. and F. S. contributed equally to this work. H. D. and F. S. conceived this work, wrote and edited the manuscript. H. D. performed theoretical analysis and numerical simulations. F. S. made conceptualization and supervised the work. H. D. and H. C. designed and implemented the experiments. Y. L., Y. Y., Z. C., S. L., and Z. W. contributed to the discussion.

#### Declaration of competing interest

The authors declare the following financial interests/personal relationships which may be considered as potential competing interests: Fei Sun reports financial support was provided by National Natural Science Foundation of China.

#### Data availability

Data will be made available on request.

#### Acknowledgements

This study was supported by the National Natural Science Foundation of China (Grant No. 61971300, 12274317, 61905208 and 62175178) and the Open Foundation of China-Belarus Belt and Road Joint Laboratory on Electromagnetic Environment Effect (No. ZBKF2022031202).

#### Appendix A. Supplementary data

Supplementary data to this article can be found online at <https://doi.org/10.1016/j.csite.2022.102587>.

#### References

- [1] B. Li, L. Wang, G. Casati, Thermal diode: rectification of heat flux, *Phys. Rev. Lett.* 93 (2004), 184301, <https://doi.org/10.1103/PhysRevLett.93.184301>.
- [2] G. Wehmeyer, T. Yabuki, C. Monachon, J. Wu, C. Dames, Thermal diodes, regulators, and switches: physical mechanisms and potential applications, *Appl. Phys. Rev.* 4 (2017), 041304, <https://doi.org/10.1063/1.5001072>.
- [3] C.W. Chang, D. Okawa, A. Majumdar, A. Zettl, Solid-state thermal rectifier, *Science* 314 (2006) 1121–1124, <https://doi.org/10.1126/science.1132898>.

- [4] N.A. Roberts, D.G. Walker, A review of thermal rectification observations and models in solid materials, *Int. J. Therm. Sci.* 50 (2011) 648–662, <https://doi.org/10.1016/j.ijthermalsci.2010.12.004>.
- [5] M.J. Martinez-Perez, A. Fornieri, F. Giazotto, Rectification of electronic heat current by a hybrid thermal diode, *Nat. Nanotechnol.* 10 (2015) 303–307, <https://doi.org/10.1038/nano.2015.11>.
- [6] L. Wang, B. Li, Thermal memory: a storage of phononic information, *Phys. Rev. Lett.* 101 (2008), 267203, <https://doi.org/10.1103/PhysRevLett.101.267203>.
- [7] J. Zhu, K. Hippalgaonkar, S. Shen, K. Wang, Y. Abate, S. Lee, J. Wu, X. Yin, A. Majumdar, X. Zhang, Temperature-gated thermal rectifier for active heat flow control, *Nano Lett.* 14 (2014) 4867–4872, <https://doi.org/10.1021/nl502261m>.
- [8] Y. Wang, A. Vallabhaneni, J. Hu, B. Qiu, Y.P. Chen, X. Ruan, Phonon lateral confinement enables thermal rectification in asymmetric single-material nanostructures, *Nano Lett.* 14 (2014) 592–596, <https://doi.org/10.1021/nl403773f>.
- [9] L. Wang, B. Li, Thermal logic gates: computation with phonons, *Phys. Rev. Lett.* 99 (2007), 177208, <https://doi.org/10.1103/PhysRevLett.99.177208>.
- [10] W. Kobayashi, Y. Teraoka, I. Terasaki, An oxide thermal rectifier, *Appl. Phys. Lett.* 95 (2009), 171905, <https://doi.org/10.1063/1.3253712>.
- [11] D. Sawaki, W. Kobayashi, Y. Moritomo, I. Terasaki, Thermal rectification in bulk materials with asymmetric shape, *Appl. Phys. Lett.* 98 (2011), 081915, <https://doi.org/10.1063/1.3559615>.
- [12] H. Wang, S. Hu, K. Takahashi, X. Zhang, H. Takamatsu, J. Chen, Experimental study of thermal rectification in suspended monolayer graphene, *Nat. Commun.* 8 (2017), 15843, <https://doi.org/10.1038/ncomms15843>.
- [13] X. Cartoixa, L. Colombo, R. Rurrali, Thermal rectification by design in Telescopic Si nanowires, *Nano Lett.* 15 (2015) 8255–8259, <https://doi.org/10.1021/acs.nanolett.5b03781>.
- [14] Z. Meng, R. Gufam, P. Zhang, F. Ma, Numerical and experimental study of the thermal rectification of a solid-liquid phase change thermal diode, *Int. J. Heat Mass Tran.* 147 (2020), 118915, <https://doi.org/10.1016/j.ijheatmasstransfer.2019.118915>.
- [15] R. Shrestha, Y. Luan, X. Luo, S. Shin, T. Zhang, P. Smith, W. Gong, M. Bockstaller, T. Luo, R. Chen, K. Hippalgaonkar, S. Shen, Dual-mode solid-state thermal rectification, *Nat. Commun.* 11 (2020) 4346, <https://doi.org/10.1038/s41467-020-18212-2>.
- [16] T. Zhang, T. Luo, Giant thermal rectification from polyethylene nanofiber thermal diodes, *Small* 11 (2015) 4657–4665, <https://doi.org/10.1002/smll.201501127>.
- [17] M.Y. Wong, B. Traipattanakul, C.Y. Tso, C.Y.H. Chao, H. Qiu, Experimental and theoretical study of a water-vapor chamber thermal diode, *Int. J. Heat Mass Tran.* 138 (2019) 173–183, <https://doi.org/10.1016/j.ijheatmasstransfer.2019.04.046>.
- [18] W. Zhao, Z. Zhu, Y. Fan, W. Xi, R. Hu, X. Luo, Temporally-adjustable radiative thermal diode based on metal-insulator phase change, *Int. J. Heat Mass Tran.* 185 (2022), 122443, <https://doi.org/10.1016/j.ijheatmasstransfer.2021.122443>.
- [19] S. Kommandur, R.A. Kishore, C. Booten, S. Cui, L.M. Wheeler, J. Vidal, Dual phase change thermal diodes with high rectification for thermal management near room temperature, *Adv. Mater. Technol-US.* 7 (2022), 2101060, <https://doi.org/10.1002/admt.202101060>.
- [20] Y. Li, X. Shen, Z. Wu, J. Huang, Y. Chen, Y. Ni, J. Huang, Temperature-dependent transformation thermotics: from switchable thermal cloaks to macroscopic thermal diodes, *Phys. Rev. Lett.* 115 (2015), 195503, <https://doi.org/10.1103/PhysRevLett.115.195503>.
- [21] S. Huang, J. Zhang, M. Wang, W. Lan, R. Hu, X. Luo, Macroscale thermal diode-like black box with high transient rectification ratio, *ES Energy Environ* 6 (2019) 51–56, <https://doi.org/10.30916/esee8c330>.
- [22] C.Y. Tso, C.Y.H. Chao, Solid-state thermal diode with shape memory alloys, *Int. J. Heat Mass Tran.* 93 (2016) 605–611, <https://doi.org/10.1016/j.ijheatmasstransfer.2015.10.045>.
- [23] Y. Li, W. Li, T. Han, X. Zheng, J. Li, B. Li, S. Fan, C.W. Qiu, Transforming heat transfer with thermal metamaterials and devices, *Nat. Rev. Mater.* 6 (2021) 488–507, <https://doi.org/10.1038/s41578-021-00283-2>.
- [24] X. Chen, Z. Xie, W. Zhou, L. Tang, K. Chen, Thermal rectification and negative differential thermal resistance behaviors in graphene/hexagonal boron nitride heterojunction, *Carbon* 100 (2016) 492–500, <https://doi.org/10.1016/j.carbon.2016.01.045>.
- [25] T. Ouyang, Y. Chen, Y. Xie, X.L. Wei, K. Yang, P. Yang, J. Zhong, Ballistic thermal rectification in asymmetric three-terminal graphene nanojunctions, *Phys. Rev. B* 82 (2010), 245403, <https://doi.org/10.1103/PhysRevB.82.245403>.
- [26] X. Chen, M. Pang, T. Chen, D. Du, K. Chen, Thermal rectification in asymmetric graphene/hexagonal boron nitride van der Waals heterostructures, *ACS Appl. Mater. Interfaces* 12 (2020) 15517–15526, <https://doi.org/10.1021/acsm.9b22498>.
- [27] M. Kasprzak, M. Sledzinska, K. Zaleski, I. Iatsunskyi, F. Alzina, S. Volz, C.M. Sotomayor Torres, B. Graczykowski, High-temperature silicon thermal diode and switch, *Nano Energy* 78 (2020), 105261, <https://doi.org/10.1016/j.nanoen.2020.105261>.
- [28] M. Schmoltz, J. Maier, E. Scheer, P. Leiderer, A thermal diode using phonon rectification, *New J. Phys.* 13 (2011), 113027, <https://doi.org/10.1088/1367-2630/13/11/113027>.
- [29] C.R. Otey, W.T. Lau, S. Fan, Thermal rectification through vacuum, *Phys. Rev. Lett.* 104 (2010), 154301, <https://doi.org/10.1103/PhysRevLett.104.154301>.
- [30] B.F. Donovan, R.J. Warzoha, Theoretical paradigm for thermal rectification via phonon filtering and spectral confinement, *Phys. Rev. Lett.* 124 (2020), 075903, <https://doi.org/10.1103/PhysRevLett.124.075903>.
- [31] H.S. Choe, R. Prabhakar, G. Wehmeyer, F.I. Allen, W. Lee, L. Jin, Y. Li, P. Yang, C.W. Qiu, C. Dames, M. Scott, A. Minor, J.H. Bahk, J. Wu, Ion write microthermatics: programing thermal metamaterials at the microscale, *Nano Lett.* 19 (2019) 3830–3837, <https://doi.org/10.1021/acs.nanolett.9b00984>.
- [32] S. Varga, A.C. Oliveira, C.F. Afonso, Characterisation of thermal diode panels for use in the cooling season in buildings, *Energy Build.* 34 (2002) 227–235, [https://doi.org/10.1016/S0378-7788\(01\)00090-1](https://doi.org/10.1016/S0378-7788(01)00090-1).
- [33] I. Hernández-Pérez, G. Álvarez, J. Xamán, I. Zavala-Guillén, J. Arce, E. Simá, Thermal performance of reflective materials applied to exterior building components-A review, *Energy Build.* 80 (2014) 81–105, <https://doi.org/10.1016/j.enbuild.2014.05.008>.
- [34] K.J. Chu, S.K. Chou, W.M. Yang, J. Yan, Achieving better energy-efficient air conditioning - a review of technologies and strategies, *Appl. Energy* 104 (2013) 87–104, <https://doi.org/10.1016/j.apenergy.2012.10.037>.
- [35] F. Riaz Siddiqui, C. Tso, H. Qiu, C.Y.H. Chao, S. Chung Fu, Hybrid nanofluid spray cooling performance and its residue surface effects: toward thermal management of high heat flux devices, *Appl. Therm. Eng.* 211 (2022), 118454, <https://doi.org/10.1016/j.applthermaleng.2022.118454>.
- [36] F. Sun, Y. Liu, Y. Yang, Z. Chen, S. He, Thermal surface transformation and its applications to heat flux manipulations, *Opt Express* 27 (2019) 33757–33767, <https://doi.org/10.1364/OE.27.033757>.
- [37] S. Guenneau, C. Amra, D. Veynante, Transformation thermodynamics: cloaking and concentrating heat flux, *Opt Express* 20 (2012) 8207–8218, <https://doi.org/10.1364/OE.20.008207>.
- [38] H. Chen, F. Sun, B. Wang, Y. Liu, Z. Chen, Y. Yang, Thermal camouflages based on 3D thermal-null medium, *Int. J. Therm. Sci.* 176 (2022), 107506, <https://doi.org/10.1016/j.ijthermalsci.2022.107506>.
- [39] R. Hu, S. Zhou, Y. Li, D.Y. Lei, X. Luo, C.W. Qiu, Illusion thermotics, *Adv. Mater.* 30 (2018), 1707237, <https://doi.org/10.1002/adma.201707237>.
- [40] T. Han, J. Zhao, T. Yuan, D.Y. Lei, B. Li, C. Qiu, Theoretical realization of an ultra-efficient thermal-energy harvesting cell made of natural materials, *Energy Environ. Sci.* 6 (2013) 3537–3541, <https://doi.org/10.1039/c3ee41512k>.
- [41] H. Barati Sedeh, M.H. Fakheri, A. Abdolali, F. Sun, Y. Ma, Feasible thermodynamics devices enabled by thermal-null medium, *Phys. Rev. Appl.* 14 (2020), 064034, <https://doi.org/10.1103/PhysRevApplied.14.064034>.
- [42] Y. Liu, F. Sun, S. He, Fast adaptive thermal buffering by a passive open shell based on transformation thermodynamics, *Adv. Theory Simu.* 1 (2018), 1800026, <https://doi.org/10.1002/adts.201800026>.
- [43] F. Yang, B. Tian, L. Xu, J. Huang, Experimental demonstration of thermal Chameleonlike rotators with transformation-invariant metamaterials, *Phys. Rev. Appl.* 14 (2020), 054024, <https://doi.org/10.1103/PhysRevApplied.14.054024>.
- [44] K. Stephan, A. Laesecke, The thermal conductivity of fluid air, *J. Phys. Chem. Ref. Data* 14 (1985) 227, <https://doi.org/10.1063/1.555749>.
- [45] C.W. Nan, R. Birringer, D.R. Clarke, H. Gleiter, Effective thermal conductivity of particulate composites with interfacial thermal resistance, *J. Appl. Phys.* 81 (1997) 6692–6699, <https://doi.org/10.1063/1.365209>.

- [46] J.P. Moore, D.L. McElroy, R.S. Graves, Thermal conductivity and electrical resistivity of high-purity copper from 72 to 400°K, *Can. J. Phys.* 45 (1967) 3849–3865, <https://doi.org/10.1139/p67-323>.
- [47] B. Doğan, H. Tan, The numerical and experimental investigation of the change of the thermal conductivity of expanded polystyrene at different temperatures and densities, *Int. J. Polym. Sci.* 2019 (2019), 6350326, <https://doi.org/10.1155/2019/6350326>.
- [48] F. Chen, D. Lei, Experimental realization of extreme heat flux concentration with easy-to-make thermal metamaterials, *Sci. Rep.* 5 (2015), 11552, <https://doi.org/10.1038/srep11552>.
- [49] F. Cardarelli, *Materials Handbook: A Concise Desktop Reference*, Springer International Publishing, 2018.
- [50] K. Yang, C. Chung, C. Tu, C. Wong, T. Yang, M. Lee, Thermal spreading resistance characteristics of a high power light emitting diode module, *Appl. Therm. Eng.* 70 (2014) 361–368, <https://doi.org/10.1016/j.applthermaleng.2014.05.028>.
- [51] T. Feng, J. Xu, An analytical solution of thermal resistance of cubic heat spreaders for electronic cooling, *Appl. Therm. Eng.* 24 (2004) 323–337, <https://doi.org/10.1016/j.applthermaleng.2003.07.001>.